









The Evolution of Binaries Embedded Within Common Envelopes

ALEJANDRA ROSSELLI-CALDERON ¹, RICARDO YARZA ^{1,2,*}, ARIADNA MURGUIA-BERTHIER ^{3,†}, VALERIA ROHOZA ^{3,1},
ROSA WALLACE EVERSON ^{1,‡}, ANDREA ANTONI ⁴, MORGAN MACLEOD ⁵ AND ENRICO RAMIREZ-RUIZ ¹

¹Department of Astronomy and Astrophysics, University of California, Santa Cruz, CA 95064, USA

²Texas Advanced Computing Center, University of Texas, Austin, TX 78759, USA

³Center for Interdisciplinary Exploration & Research in Astrophysics (CIERA), Evanston, IL 60202, USA

⁴Astronomy Department and Theoretical Astrophysics Center, University of California, Berkeley, CA 94720, USA

⁵Institute for Theory & Computation, Center for Astrophysics, Harvard & Smithsonian, Cambridge, MA, USA

ABSTRACT

Triple stellar systems allow us to study stellar processes that cannot be attained in binary stars. The evolutionary phases in which the stellar members undergo mass exchanges can alter the hierarchical layout of these systems. Yet, the lack of a self-consistent treatment of common-envelope (CE) in triple star-systems hinders the comprehensive understanding of their long-term fate. This letter examines the conditions predicted around binaries embedded within CEs using local 3D hydrodynamical simulations. We explore varying the initial binary separation, the flow Mach number, and the background stellar density gradients as informed by a wide array of CE conditions, including those invoked to explain the formation of the triple system hosting PSR J0337+1715. We find that the stellar density gradient governs the gaseous drag force, which determines the final configuration of the embedded binary. We observe a comparable net drag force on the center of mass but an overall reduction in the accretion rate of the binary compared to the single object case. We find that for most CE conditions, and in contrast to the uniform background density case, the binary orbital separation increases with time, softening the binary and preventing it from subsequently merging. We conclude that binaries spiraling within CEs become more vulnerable to be disrupted by tidal interactions. This can have profound implications on the final outcomes of triple star-systems.

Keywords: common envelope- hydrodynamical simulations, triple systems

1. INTRODUCTION

Field stars are commonly formed in pairs, and many of these binaries are part of triples or even higher-order arrangements (Bonnell et al. 2003; Moe & Di Stefano 2017). Even though the basics of single stellar evolution and binary evolution have been established for a long time, many aspects of triple star evolution remain mysterious (Toonen et al. 2016). Triples are of general interest as progenitor avenues for LIGO binaries (Vigna-Gómez et al. 2021), which are spectacular probes of the extreme physics at high energy and high density, being strong gravitational-wave sources. They have been found to harbor millisecond pulsars (Ransom et al. 2014), and as such are ideal test-beds of strong-field tests of general relativity and alternative theories of gravity (Archibald et al. 2018).

Observed stable triple systems are mostly found in a hierarchical arrangement. These systems are composed of two

closely orbiting stars in an inner binary, hereafter referred to as the binary, and an outer star in a wider orbit about the center of mass of the inner binary. For the cases explored in this *Letter*, the outermost star is the more massive of the three, and hereafter will be called the primary. A critical juncture in the life of a triple star is the period just after mass transfer commences in the system (Toonen et al. 2016; Comerford & Izzard 2020; Michaely & Perets 2019; Soker & Bear 2021). The system either merges or may survive to become an interacting triple. When mass transfer is unstable, the inner binary is thought to shrink mainly during a phase of unstable mass transfer. The envelope of the donor star, during this common envelope (CE) phase, engulfs both stars causing the binary to spiral inwards.

The embedded binary spirals to tighter orbital separations under the influence of drag from the surrounding envelope material. This gravitational drag force deposits orbital kinetic energy into the envelope and is expected to influence the orbit of the infalling binary, whose orbital evolution remains poorly understood. If the embedded binary spirals deep enough within the envelope of the evolving star, it can deposit sufficient energy to unbind the entire hydrogen envelope (Comerford & Izzard 2020). The outcome of this enve-

* NASA FINESST Fellow
Frontera Computational Science Fellow

† Einstein Fellow

‡ NSF Graduate Research Fellow

lope ejection can lead to the core of the evolving star placed in a substantially tightened triple system or binary system if one of the binary members is tidally ejected. The millisecond pulsar triple system PSR J0337+1715 has been theorized to be one of such systems where a CE phase could have played a significant role in its evolution and final outcome. (Tauris & van den Heuvel 2014; Sabach & Soker 2015; Lagos et al. 2023). This system is used here to guide our simulation work.

The detailed understanding of binaries within a CE remains largely unexplored (Toonen et al. 2016; Comerford & Izzard 2020) primarily because the interaction is governed by intertwined physical processes on a large range of scales (Glanz & Perets 2021a,b). The governing timescales range from the stellar evolutionary timescale that establishes the initial conditions of a binary interaction to the dynamical timescale of flow near an embedded object’s surface. These challenges imply that global simulations can not effectively capture the full range of physical processes that determine the evolution of a binary system during a CE interaction.

A specific concern is the resolution constraints of simulating the full spatial range of the embedded binary for many orbital timescales indicates that the calculations are either highly computationally expensive, or they are achieved with exceedingly low numerical resolution. In this *Letter*, we adopt the complementary method of simulating a well-defined, but idealized scenario. We study the flow past a binary system in the context of a wind tunnel numerical setup, detailed in Section 3 (MacLeod & Ramirez-Ruiz 2015a; MacLeod et al. 2017a; Antoni et al. 2019). To determine the conditions of the flow, we consider stellar structures (and gas adiabatic exponents) appropriate to a wide range of regimes of CE interactions in hierarchical triples. By restricting the scope of the problem, this idealized approach allows us to, for the first time, study the orbital evolution of the embedded binary.

This *Letter* is organized as follows. In Section 2, we review the key descriptive parameters for CE flows and discuss the relevant range of values with a particular emphasis on the assembly of the remarkable triple system hosting PSR J0337+1715. These flow properties are used to inform the setup of our numerical experiments. Section 3 describes our numerical method while Section 4 examines the results of a set of numerical experiments. Section 5 summarizes the implications that these idealized results have for our understanding of the evolution of embedded binary systems undergoing typical CE interaction.

2. FLOW CONDITIONS AND A CASE STUDY

When modeling the flow around the embedded binary, we parameterize the properties of the gas using the formalism developed by MacLeod & Ramirez-Ruiz (2015a,b) and MacLeod et al. (2017a). The setup of the problem is as follows. We have a primary star with total mass M and radius R that engulfs its two less massive companions m_1 and m_2 , arranged in a close binary. We study the case where $m_1 = m_2$ and define the total mass of the binary system as

$m = m_1 + m_2$. The separation between m_1 and m_2 is given by a_0 . The distance between the center of mass of the binary and the center of mass of the primary is defined as a , where $a \lesssim R$. For the cases relevant to this study, $a_0 < R$, which ensures that both members of the binary are embedded within the primary’s stellar envelope. This is expected to be the case for most triples, which are observed to have hierarchical structures (Toonen et al. 2016). We define the mass ratio between the primary and the embedded binary system as $q = m/M$. In this section, we explore the general conditions of the flow and provide the reader with flow parameters relevant to the assembly history of PSR J0337+1715.

2.1. Flow Properties during CE

The flow can be contextualized with the characteristic scales of a Bondi-Hoyle (BH) accretion (Hoyle & Lyttleton 1939; Bondi & Hoyle 1944). The accretion capture radius R_a of the binary can be written as

$$R_a = \frac{2Gm}{v_\infty^2} \quad (1)$$

for supersonic flows, where m is the total mass of the binary and v_∞ is the relative velocity of the center of mass of the binary system and its surrounding medium (Antoni et al. 2019). The accretion capture radius will inform the rate of accretion of the two stars. The Mach number of the flow is $\mathcal{M}_\infty = v_\infty/c_{s,\infty} \gtrsim 1$, where $c_{s,\infty}$ is the sound speed of the gas. These imply an accretion rate onto the embedded binary,

$$\dot{m}_{\text{BH}} = \pi R_a^2 \rho_\infty v_\infty \left(\frac{\mathcal{M}_\infty^2}{1 + \mathcal{M}_\infty^2} \right)^{3/2}, \quad (2)$$

where ρ_∞ describes the characteristic background density. The associated orbital energy decay rate is then

$$\dot{E}_{\text{BH}} = \frac{\pi}{2} R_a^2 \rho_\infty v_\infty^3 \left(\frac{\mathcal{M}_\infty^2}{1 + \mathcal{M}_\infty^2} \right)^{1/2}, \quad (3)$$

which leads to a characteristic stopping timescale of,

$$\tau_{\text{stop,BH}} = \frac{\frac{1}{2} m v_\infty^2}{\dot{E}_{\text{BH}}} = \frac{v_\infty^3}{4\pi G^2 m \rho_\infty} \left(\frac{\mathcal{M}_\infty^2}{1 + \mathcal{M}_\infty^2} \right)^{1/2}. \quad (4)$$

The orbital energy decay will trace slow down the center of mass of the binary. The characteristic orbital velocity of the binary system around the primary star is

$$v_k = \sqrt{\frac{G(M+m)}{a}} \quad (5)$$

In general, $v_\infty \approx v_k$ such that $\tau_{\text{stop,BH}} \approx (E_{\text{orb}}/\dot{E}_{\text{BH}})$ confers the radial sinking timescale of the binary in the stellar envelope, where we have assumed that the mean stellar density enclosed by the orbit is $\approx \rho_\infty$. The motion of the embedded binary might be, however, desynchronized from the primary’s gaseous envelope and the relative velocity can be

written as $v_\infty = f_k v_k$, where f_k is the fraction of Keplerian velocity that describes the relative motion between the center of mass of the binary and the gas. R_a can then be expressed as

$$\frac{R_a}{a} = \frac{2}{f_k^2} \frac{m}{(M+m)} = \frac{2}{f_k^2} \frac{1}{(1+q^{-1})} \quad (6)$$

In the case of $f_k = 1$ and $M \gg m$, then $(R_a/a) \approx 2q$. It is important to note that when the enclosed primary-star mass, $M(a)$ is considerably less than M , one needs to use $q_{\text{enc}} = m/M(a)$ in place of q in Equation 6.

Another characteristic length scales that plays a key role in defining the CE interaction is the density scale height (MacLeod & Ramirez-Ruiz 2015a,b) which depends on the structure of the primary star and is given by

$$H_\rho = -\rho \frac{dr}{d\rho}. \quad (7)$$

For the case of the embedded binary, we measure H_ρ at the center of mass of the system. For simplicity, we define a dimensionless parameter ε_ρ to describe the number of density scale heights encapsulated by the accretion radius,

$$\varepsilon_\rho \equiv \frac{R_a}{H_\rho}. \quad (8)$$

For the case of a binary moving through a uniform density medium $\varepsilon_\rho = 0$, while $\varepsilon_\rho \gtrsim 1$ describes relatively steep stellar density gradients (MacLeod & Ramirez-Ruiz 2015a; Antoni et al. 2019; Everson et al. 2020). The vertical gradient, whose strength is determined by ε_ρ , provides the flow net angular momentum relative to the accreting object (Murguía-Berthier et al. 2017). Thus, we expect that even modest gradients could have sizable impacts on the evolution of the orbit of the embedded binary.

The envelope and the binary will both be subjected to the gravitational force of the primary star, which allows one to connect the properties of the CE flow on the basis of the hydrostatic equilibrium conditions of the stellar envelope (MacLeod et al. 2017a)

$$\mathcal{M}^2 = \varepsilon_\rho \frac{(1+q)^2}{2q} f_k^4 \left(\frac{\Gamma_s}{\gamma} \right), \quad (9)$$

where Γ_s is the polytropic index of the stellar profile and γ is the gas adiabatic index. This relation is particularly useful because it limits the relevant parameter space that one needs to explore numerically to effectively characterize the CE flows. In the stellar envelopes in hydrostatic equilibrium for massive stars in giant phases, the ratio of Γ_s to γ will be ≈ 1 . For a fixed f_k , we have a \mathcal{M} that depends solely on ε_ρ and q , allowing us to vary these two parameters and draw aggregate conclusions.

2.2. The Case of PSR J0337+1715

As an example of the typical flow properties expected for binaries embedded in CEs, we discuss here one of the

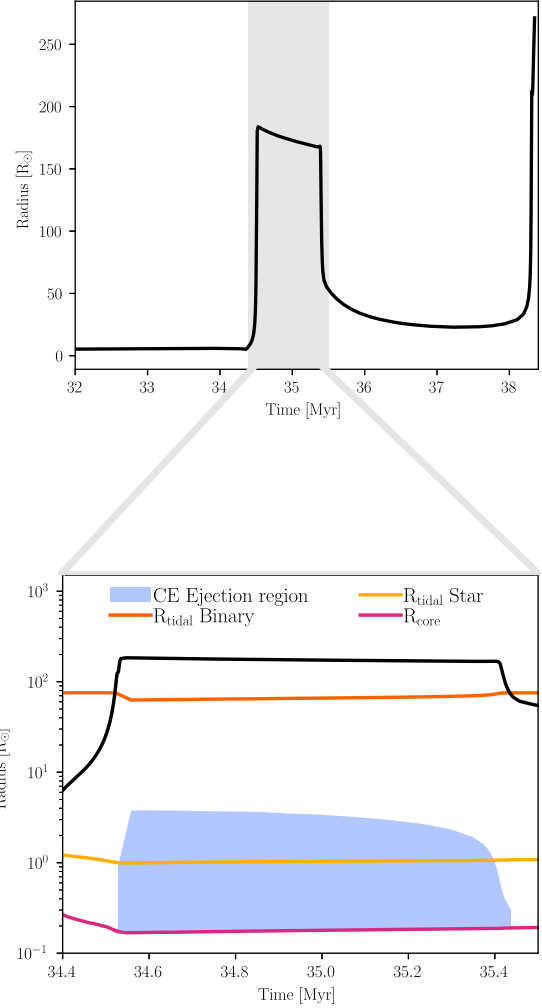


Figure 1. Profiles of primary-star stellar structure in a triple system relevant to CE interaction. *Top panel:* The MESA evolution of the radius of the $8M_\odot$ progenitor star of PSR J0337+1715 is shown as a function of time. The outer binary, assumed here to be composed of two $1M_\odot$ sun-like stars, is expected to be embedded within the envelope of the primary star provided that it resides at separations below the black vertical line (shaded region). The y-axis shows radial distance in R_\odot units. *Bottom panel:* The inner structure of the primary star as calculated by MESA. The outer radius of the star is shown by the black curve. As the binary spirals it is expected to be tidally disrupted at a radius given by the orange curve, while the yellow curve represents the tidal disruption radius of a $1M_\odot$ sun-like star. The shaded blue region represents the ranges of radii where CE ejection is possible due to a single body, since the binary has already been tidally disrupted at an outer radius. The pink curve represents the edge of the inner He core.

commonly discussed formation scenarios for the remarkable triple star system that harbors the millisecond pulsar PSR J0337+1715 (Tauris & van den Heuvel 2014; Sabach

& Soker 2015). This system is comprised of a $1.438M_{\odot}$ millisecond pulsar with a spin period of 2.73ms orbiting by two white dwarfs (Ransom et al. 2014; Archibald et al. 2018). The white dwarf member of the inner binary has a mass of $0.1975M_{\odot}$ and a semi-major axis of $0.83R_{\odot}$ while the distant white dwarf orbiting the centre of mass of the inner binary has a mass of $0.41M_{\odot}$ and a semi-major axis of $51.28R_{\odot}$.

In some triple systems, the outer star has no influence on the evolution of the inner binary, such that the evolution of the inner binary and the outer tertiary can be explained independently. In this case, it is reckoned that interactions between the three stars took place early in the evolution of the system (Tauris & van den Heuvel 2014). As the outer stellar progenitor of PSR J0337+1715’s expanded, it has been suggested that the inner sun-like pair was completely engulfed, causing the inner binary to spiral inwards (Sabach & Soker 2015). A detailed explanation, along with a schematic, of the proposed formation scenario is presented in Appendix A.

The upper panel of Figure 1 shows the evolutionary history, as envisioned by Sabach & Soker (2015), of the primary stellar progenitor of PSR J0337+1715. We use the stellar code MESA (version r23.05.01, Paxton et al. 2011, 2013, 2015, 2018, 2019; Jermyn et al. 2023) to model the evolution of the primary star, with an initial mass of $8M_{\odot}$ and with solar metallicity, from zero-age main sequence to the asymptotic giant branch. In the first stage of the evolution of the system, the primary’s envelope will embed the inner binary hosting two nearly equal sun-like stars. For simplicity we assume the binary hosts two $1M_{\odot}$ sun-like stars.

As the binary spirals inside of the primary’s envelope, it is expected to be tidally disrupted, resulting in the ejection of one of the sun-like companions. We integrate over the enclosed mass of the primary while treating the stars in the binary as point masses to calculate the radius at which the binary would become tidally disrupted. We find this disruption to occur at a radius of $\approx 70R_{\odot}$ from the core of the primary for a binary separation $a_0 = 60R_{\odot}$ (orange curve in the lower panel of Figure 1). After the binary breakup, the non-ejected companion, which is still embedded within the CE, continues to spiral in towards the primary’s core (pink curve in the lower panel of Figure 1). It is then up to this companion to aid with the ejection of the envelope, which is expected to take place within the blue shaded region in the lower panel of Figure 1. The shaded blue region is calculated using the standard α formalism (van den Heuvel 1976; Webbink 1984) and the reader is referred to Wu et al. (2020), Law-Smith et al. (2020), and Everson et al. (2023) for details on the implementation when using MESA stellar profiles.

What happens when a binary gets embedded in a CE has not been studied in great detail, as it is an inherently complicated problem where the dynamics of the binary’s orbit and the hydrodynamics of the flow need to be taken into account consistently. The case of PSR J0337+1715 offers us clear guidance of the flow properties that are usually encountered by embedded binaries. Typical flow values (Equations 8 and 9) during the CE interaction are $0.9 \lesssim \varepsilon_{\rho} \lesssim 2$ and $1.5 \lesssim \mathcal{M} \lesssim 2.5$ (Figure 7 in Appendix 7). These val-

ues are calculated from the onset of dynamical inspiral of the center of mass of the binary, which disrupts the outer layers of the envelope before CE occurs (MacLeod et al. 2017b), to the end of dynamical inspiral, which is expected to be terminated at an inner radius at which a $1M_{\odot}$ sun-like star would be tidally disrupted by the primary’s core. The reader is referred to Appendix A for details on these values for the simulated primary progenitor of PSR J0337+1715. It is important to note that these ranges are typical of those expected for the vast majority of CE encounters (Everson et al. 2020) and will be used to guide our numerical setup, which is presented in Section 3.

The system’s post-CE configuration is expected to leave the core of the primary and secondary in a close binary and the tertiary companion further out but still gravitationally bound. While the system will further evolve and additional interactions are expected to occur (Tauris & van den Heuvel 2014; Sabach & Soker 2015), we note that one of the major uncertainties in the modelling comes from the lack of understanding of the evolution of the inner sun-like pair and the poorly known orbital evolution of the binary during the CE phase.

3. NUMERICAL APPROACH

The wind tunnel is a three-dimensional, Cartesian geometry hydrodynamic simulation setup that includes the gravity of the embedded binary and the primary evolving star, which allows us to study the coefficients of drag and accretion experienced by the embedded binary. Accretion and drag lead to a transformation of both the center of mass of the binary and its orbit during a CE phase.

3.1. Wind tunnel conditions

As the upstream conditions become inhomogeneous, the symmetry that defines Bondi-Hoyle accretion is quickly broken. Instead we observe an asymmetric flow, in which the momenta of incoming fluid no longer cancel in the wake (MacLeod & Ramirez-Ruiz 2015a). These flow properties can alter the rates of drag of the sinking of the center of mass of the system and the evolution of the orbit of the embedded binary when compared with the Hoyle-Lyttleton case (Antoni et al. 2019).

We use the FLASH hydrodynamics code (Fryxell et al. 2000) to numerically solve the fluid equations. We implement FLASH’s directionally split Piecewise Parabolic Method Riemann solver (Colella & Woodward 1984). We use sinks (Federrath et al. 2010) to define the stars as point masses that accrete material from their environment and respond to the forces induced by the gas. We place two orbiting sinks in the gas medium and allow them to move freely, unconstrained to a fixed center of mass location (Antoni et al. 2019). The numerical formalism is described in detail in MacLeod et al. (2017a) but we discuss, in what follows, for context some key aspects of the problem setup.

A wind, depicting the stellar envelope of the primary star with a vertical gradient of density and pressure, is injected in the $+x$ direction from the $-x$ boundary. The profile is in

hydrostatic equilibrium with a vertical $-y$ acceleration given by gravitational influence of the enclosed mass of the primary star, which remains uniform in the z direction. The conditions of the flow are parameterized by ε_ρ , q , and the pressure and density at $y = 0$ determined by f_k , Γ_s and γ (equation 9). The values at $y = 0$ are then used to inform the vertical structure of the flow $\pm y$, which is calculated assuming hydrostatic equilibrium. In this setup we model the embedded binary ($m_1 = m_2$) as two sink point particles of radius $R_s = 0.05R_a$, whose center of mass at $t = 0$ is at rest ($\mathbf{V}_{\text{CoM}} = 0$) and placed at the origin of the grid ($\mathbf{R}_{\text{CoM}} = 0$). The binary is originally placed in a circular orbit at a distance a_0 in the $x - y$ plane with the angular momentum vector pointing in the $+z$ direction. As the system evolves in time, \mathbf{V}_{CoM} and \mathbf{R}_{CoM} change as they accrete material and interact gravitationally with each other and the background gas. The reader is referred to [Antoni et al. \(2019\)](#) for additional details on the binary implementation.

The simulations are performed in dimensionless units, where $R_a = v_\infty = \rho_\infty = 1$, where ρ_∞ is the density of the stellar envelope at a radial distance a ($y = 0$) from the center of mass of the primary star. In code units, the characteristic timescale is $R_a/v_\infty = 1$ while the mass of the embedded binary is $m = (2G)^{-1}$. Previous work has studied the effects of domain size and spatial resolution on the robustness of the numerical results for single objects embedded in CEs ([MacLeod et al. 2017a](#)) and binaries moving supersonically relative to a uniform medium ([Antoni et al. 2019](#)). Based on these studies and our own resolution study, we adopt the following bounds for our simulation runs. The computational domain is $(-3, 3)R_a \times (-3, 3)R_a \times (-3, 3)R_a$. The maximum and minimum refinement level is set to 6 and 2, respectively. Therefore, the maximum cell size is $R_a/16$ and the minimum is $R_a/256$.

The parameters that we vary in the simulations are selected to investigate the evolution of embedded CE binaries with a range of orbital periods and experiencing a wide range of stellar density gradients. As such, we change ε_ρ and a_0 between 0 and 2.0, and 0.16 to 1.0, respectively. Throughout the simulations we assume $\Gamma_s = \gamma = 5/3$ ([Everson et al. 2020](#)) and perform calculations with $q = 0.1$ and $q = 0.15$ (Section 2.2). By selecting q and ε_ρ , the upstream Mach number (\mathcal{M}_∞) can be computed employing Equation (9). The use of dimensionless flow parameters in our simulations allows for the results of this study to be broadly applicable to a wide range of embedded binaries (Section C in the Appendix). This is because the properties of the flow throughout CE encounters are self-similar across a broad range of post-main-sequence primary masses, evolutionary stages, mass ratios and metallicities ([Everson et al. 2020](#)).

3.2. Quantifying the role of drag and mass accretion

The evolution of the embedded binary depends sensitively on gas drag and mass accretion, which slows the center of mass and alters orbital spiraling. When the gas approaches the boundaries of a sink, it gets accreted. The accretion step is performed by integrating a quantity, either mass or mo-

mentum, over all cells within the volume of the sink and then adding these summed values to the particle’s properties ([Antoni et al. 2019](#)). To compute the rate of accretion, we then divided the accreted quantity by the time step. The accretion rate is saved and then the gas is deleted by resetting the density within the sink to $\rho_{\text{sink}} = 10^{-2}\rho_\infty$ as well as setting the velocity components of the gas to zero. The mass accretion rate is calculated as a volume integral over a sink i such that:

$$\dot{m}_i = \frac{1}{\Delta t} \int_{\text{sink}_i} (\rho - \rho_{\text{sink}}) dV. \quad (10)$$

The total accretion rate of the binary is then the sum of the individual accretion rates of the sinks, $\dot{m} = \dot{m}_1 + \dot{m}_2$.

The accretion for the linear momentum of the gas onto the sink is integrated in each Cartesian coordinate as,

$$\dot{\mathbf{p}}_i = \frac{1}{\Delta t} \int_{\text{sink}_i} \mathbf{v}(\rho - \rho_{\text{sink}}) dV. \quad (11)$$

The accretion of linear momentum will exert a force on the sinks. We call these forces “momentum transport forces” and denote them as $\mathbf{F}_{\dot{p}_1}$ and $\mathbf{F}_{\dot{p}_2}$, acting on m_1 and m_2 respectively ([Antoni et al. 2019](#)). The net momentum transfer force on the center of mass of the binary will be defined as,

$$\mathbf{F}_{\dot{p}} = \mathbf{F}_{\dot{p}_1} + \mathbf{F}_{\dot{p}_2}. \quad (12)$$

As the sinks evolve over time, they exert a gravitational force on the surrounding gas. These forces cause the gas to get redistributed. In response to this, the gas exerts a gravitational force on each of the members of the binary. The total force on each member can be found by summing over the contributions of each of the cells in the domain. Using \mathbf{r}_i as the location of a particle m_i in the domain and \mathbf{r}' as the location of a particular gas cell, we can find the force on m_i due to the cell as,

$$d\mathbf{F}_{\text{DF}_i} = -\frac{Gm_i\rho(\mathbf{r}')dV}{|\mathbf{r}_i - \mathbf{r}'|^3}(\mathbf{r}_i - \mathbf{r}'). \quad (13)$$

We take the integral over a sphere of volume V with center at the center of mass of the binary to find the total gas drag force on m_i ,

$$\mathbf{F}_{\text{DF}_i} = -\int_V \frac{Gm_i\rho(\mathbf{r}')dV}{|\mathbf{r}_i - \mathbf{r}'|^3}(\mathbf{r}_i - \mathbf{r}'). \quad (14)$$

The net gas drag force on the center of mass is,

$$\mathbf{F}_{\text{DF}} = \mathbf{F}_{\text{DF}_1} + \mathbf{F}_{\text{DF}_2}. \quad (15)$$

The position and corresponding velocity of each particle are updated to account for the accreted material. Before the gas is evolved further, each particle’s motion is advanced using the active sink particles leapfrog integrator ([Antoni et al. 2019](#)). At each time step, we document the accretion rates and forces in addition to the position, total mass, position, and velocity of each particle.

4. NUMERICAL RESULTS

Our study aims to address questions surrounding the morphology and structure of flows in the vicinity of a binary embedded within a CE, the relative rates of drag and accretion, and how those flows influence the orbital evolution of the embedded system. These results are compared for robustness with those from a single object embedded within a CE ($a_0 = 0$) and a binary moving supersonically relative to a uniform medium ($\varepsilon_\rho = 0$), which have been extensively studied by MacLeod et al. (2017a) and Antoni et al. (2019), respectively.

4.1. Binaries embedded in CEs

We begin examining the contributions of the gas dynamical friction and the accretion of linear momentum by the sink boundaries to the net drag force. The effect on the binary is compared with the case in which the system is replaced by an effective star at the center of mass of the binary ($a_0 = 0$). For this set of simulations, the initial separation of the binary is set to $a_0 = 0.42R_a$, the density gradient parameter is $\varepsilon_\rho = 0.3$ and the Mach number $\mathcal{M} \approx 1.0$. Figure 2 shows the net drag forces including contributions from dynamical friction (Equation 15) and accretion of linear momentum (Equation 12) projected onto the velocity of the center of mass vector. The solid lines in the left panel of Figure 2 shows the net force on the center of mass of the binary while the dotted line shows the net force on the effective single mass object. The gravitational drag force, given by Equation 15, is integrated over four different volumes each timestep following the procedure described in MacLeod et al. (2017a). The integration volumes are selected to be spherical shells with their inner radii placed at the center of mass of the binary and varying outer radii between $0.78R_a$ and $3R_a$. The different colors in the left panel of Figure 2 correspond to different outer radius (r_{out}). As expected, the gas dynamical friction forces grows as $\propto \ln(r_{\text{out}})$.

Figure 2 shows that the average net force on the binary and on the single effective point mass are commensurate when embedded in the same CE flow. In general, the flow morphology becomes less laminar when the binary is present. Predictably, the binary case shows modulations on the net force induced by its orbital motion. The periodic flow disturbances induced by the binary, which propagate at large distances, modify the density distribution around the bow shock region. These gas disturbances are clearly seen in the flow visualizations of Figures 3 and 10. The single point mass case, on the other hand, generates a stable bow shock structure once steady state is achieved (MacLeod et al. 2017a). The density disturbances of the flow at large radii as induced by the binary lead to a slight decrease in the gas drag force when compare to the single point mass case (see differences between dotted lines and solid lines in the right panel of Figure 2).

Our numerical approach substitutes the binary stellar members with sinks on the grid, which absorb the convergent flow. As such, we investigate the properties of gas accreting through this inner boundary and note that the accretion rate is

reliant on the size of the sink (MacLeod et al. 2017a; Antoni et al. 2019). The right panel of Figure 2 shows the total mass accretion rate for both the binary (*dark blue*) and the effective single point mass (*light blue*). The accretion rate of the binary is the sum of the individual accretion rates for each of the stellar members. The time dependent accretion rates are delineated by the fainter lines while the median values are depicted by the bold lines. The mass accretion rate for the single point mass is consistent with the values derived by MacLeod et al. (2017a) and is higher than the accretion rate of the binary. This is because at the chosen binary separation ($a_0 = 0.42R_a$), the effective cross section of the single point mass is larger by about 20%. This is because in the limit when $a_0 \gtrsim R_a$, the binary system evolves accordingly to the prescription for two independent objects (each of mass $\frac{1}{2}m$). In this limit, we would expect the accretion rate of the system to be $\propto (m_1^2 + m_2^2) = m^2/2$. Having demonstrated that the net drag force on the center of mass of the binary closely tracks the drag behavior of the single object case, in what follows we investigate the impact that ε_ρ has on the evolution of the binary.

4.2. The role of ε_ρ

As density gradients steepen, we thus expect the accretion rate to decrease and the net drag force to increase (MacLeod et al. 2017a). Figure 3 illustrates the effects of varying ε_ρ for a binary with $a_0 = 0.42R_a$ and $q = 0.15$, corresponding to $\mathcal{M} \approx 1.5, 2.0, 3.0$ for $\varepsilon_\rho = 0.5, 1, 2$ respectively. Three values of ε_ρ , which are representative of CE flows (Figure 1), are displayed: 0.5, 1, and 2. Our simulations are consistent with the flow properties studied by MacLeod et al. (2017a). For a relatively shallow density gradient ($\varepsilon_\rho = 0.5$), the symmetry of the bow shock is just about maintained. As the density gradient steepens, the material focused onto the wake comes from material originating deeper within the stellar envelope, altering the shock morphology.

The bottom left panel in Figure 3 shows the net force on the center of mass of the binary. Here, we add the momentum transfer force on each of the sinks and the gaseous drag force integrated up to a distance $3.0R_a$. As in MacLeod et al. (2017a), the total drag force is observed to augment with increasing ε_ρ . This is because the drag force depends not only on the value of the density (ρ_∞) at the position of the center of mass of the binary (Antoni et al. 2019) but also the mass redistribution within the accretion radius. As ε_ρ increases, dense material from deeper within the stellar envelope is focused into the wake of the embedded binary, causing it to provide an increasing contribution to the net dynamical friction.

We now consider the forces impacting the motion of the binary about the center of mass. In the bottom right panel of Figure 3, we show the change in the binary separation, $\Delta a(t) = a(t) - a_0$, as function of simulation time. The periodic deviations around the mean value are caused by the changing direction of the barycentric velocities over each single orbit. As in Antoni et al. (2019), gaseous drag forces can cause a tightening of the orbit when the density gradi-

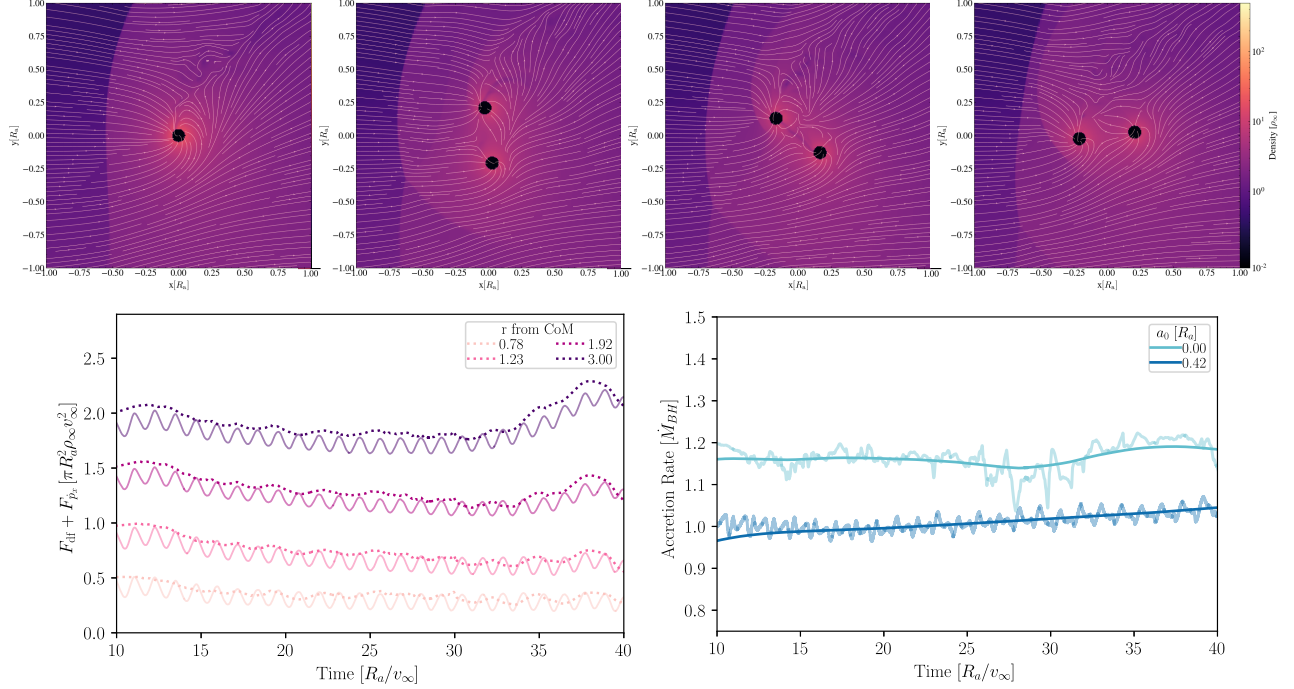


Figure 2. Net drag force (with contributions from dynamical friction and accretion of linear momentum) projected along the direction of the center of mass velocity vector and mass accretion rate as a function of simulation time for a binary embedded in a CE flow. The simulation parameters are $a_0 = 0.42R_a$, $\varepsilon_\rho = 0.3$, and $\mathcal{M} \approx 1.0$. The period of the binary is $\sim 1.2R_a/v_\infty$. The effect on the binary is compared with that on a single point mass ($a_0 = 0$). *Top left panel:* Flow morphology for a single point mass. *Top rightmost three panel:* Flow morphology for the binary case at three different times increasing from left to right. Density slices are taken for $z = 0$ plane surrounding the sinks. *Bottom left panel:* Net drag force on the center of mass of the binary. The solid line shows the net force on the binary while the dotted line shows the net force on the single mass particle. The different colors denote the distance from the center of mass to the integration radius. *Bottom right panel:* Mass accretion rate for the single point mass and total accretion rate for the two sinks in the case of the binary. Lighter lines show the rate at each time step and darker lines show the median values. The variations in the mass accretion rates are mainly driven by the periodic motion of the binary, which in turn modifies the density structure of the flow.

ent is shallow ($\varepsilon_\rho = 0.5$). This is because the convergence of the gravitationally focused gas leads to a central density enhancement (when compared to ρ_∞) in and around the binary orbit. As the density gradient steepens, material originating from deeper within the stellar envelope notably alters the density distribution of the bow shock region. As a result, the scaling from the gaseous drag forces evolves from a tightening to a softening of the binary at a critical ε_ρ , which as we discuss in Section 4.4 depends also sensitively on q .

4.3. Key Timescales

A binary embedded in a CE will evolve as a result of drag and accretion. Forces on the center of mass lessen the kinetic energy content of the system, E_{trans} , over a timescale τ_{stop} . The orbit-averaged decrease in kinetic energy content, $\langle \dot{E}_{\text{trans}} \rangle$, causes the sinking of the center of mass of the binary over a timescale

$$\langle \tau_{\text{stop}} \rangle \equiv \frac{E_{\text{trans}}}{\langle \dot{E}_{\text{trans}} \rangle}. \quad (16)$$

Forces on the binary orbit modify the separation over a timescale τ_{insp} . Both drag and momentum transport cause

a net drag on the orbital motion. The orbit-averaged inspiral timescale can thus be written as

$$\langle \tau_{\text{insp}} \rangle \equiv \frac{-a_0}{\langle \dot{a} \rangle}, \quad (17)$$

where $\langle \dot{a} \rangle$ is calculated by taking the median over an integer number of orbits during the simulation. The sign of the timescale was chosen to be compatible with Antoni et al. (2019). For a binary that tightens $\tau_{\text{insp}} > 0$ while for softening binaries $\tau_{\text{insp}} < 0$. The magnitude of τ_{insp} is thus a measure for how quickly the tightening or softening of the binary orbit takes place. For non-evolving binaries, $\tau_{\text{insp}} \rightarrow \infty$ or equivalently $\tau_{\text{insp}}^{-1} \rightarrow 0$. In this section we explore these timescales and their hierarchy, which will determine how a triple system evolves.

The sinking timescale of the center of mass inside the envelope, τ_{stop} , will determine how swiftly the binary reaches its tidal radius as it approaches the primary's He core. We find that τ_{stop} is primarily determined by the properties of the flow (q and ε_ρ). Similar to the $\varepsilon_\rho = 0$ case (Antoni et al. 2019), we find $\tau_{\text{stop}} < \tau_{\text{insp}}$ for $\varepsilon_\rho = 0.5$ and a systematic

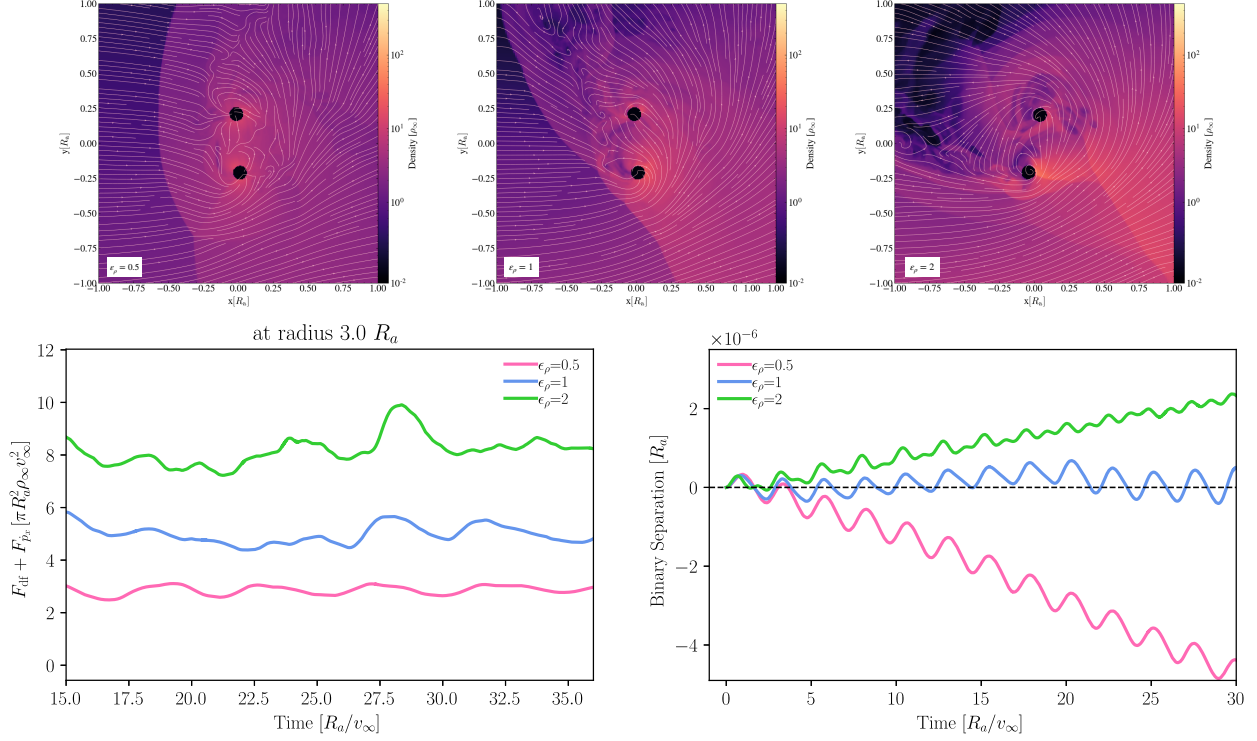


Figure 3. Diagnostics of CE Flow Properties. *Top panels:* Flow morphology for a binary with $a_0 = 0.42$ and $q = 0.15$ embedded in a CE flow with varying stellar density gradients. Density slices through the $z = 0$ plane surrounding the binary. From left to right $\varepsilon_\rho = 0.5, 1.0, 2.0$. *Bottom left panel:* The net drag force on the center of mass of the binary projected onto the velocity of the center of mass vector, including contributions from dynamical friction, \mathbf{F}_{df} , and accretion of linear momentum, \mathbf{F}_p . The drag forces are integrated over a spherical domain up to a radius $3.0 R_a$ from the center of mass of the binary. *Bottom right panel:* The change in the binary separation, $\Delta a(t) = a(t) - a_0$, as function of simulation time in units of R_a . For the case of a steep ε_ρ , the binary separation increases over time while for a shallower ε_ρ the separation decreases, as also found in the case of $\varepsilon_\rho = 0$ (Antoni et al. 2019).

decrease in τ_{stop} with increasing ε_ρ , as found in MacLeod et al. (2017a) for the $a_0 = 0$ case. The reader is referred to Figure 8 and Appendix B for a more in depth presentation and discussion of our results, respectively.

Figure 4 depicts the dependence of τ_{insp} as a function of a_0 for both shallow and steep stellar density gradient models. We calculate the a_0 -dependence of τ_{insp} by perform a least-squares fit to a power law of the form $\propto (a_0/R_a)^B$. The shallow density gradient models ($\varepsilon_\rho = 0.5$) are compared with the scaling of τ_{insp} with a_0 of $B \approx 0.19$ derived by Antoni et al. (2019) for $\varepsilon_\rho = 0$. The orbital evolution with separation thus follows the scaling found for a constant density medium although the orbit-averaged torques are weaker. We find that for shallow density gradients, the inspiral timescale ($\tau_{\text{insp}} > 0$) decreases with a such that the system will merge if given enough time.

In contrast, for steep density gradients ($\varepsilon_\rho = 2.0$), the separation of the binary is found to increase with time ($\tau_{\text{insp}} < 0$) at all separations. As such, we expect the binary will widen as it sinks into the surrounding envelope. As the binary separation increases, the orbital speed of each object decreases, augmenting the total outward torque. In other words, as the binary softens, the magnitude of τ_{insp} becomes pro-

gressively less negative, which implies that binary expansion is gradually accelerated. For $\varepsilon_\rho = 2.0$ we find $B \approx -1.1$ (Figure 4).

4.4. The hardening or softening of binaries during CE

In what follows we further explore the conditions for which τ_{insp} reverts sign in the (ε_ρ, a_0) plane. In the simulation results presented in Figure 4 we fix $q = 0.15$ and vary a_0 and ε_ρ . Shown is the orbit-averaged frequency τ_{insp}^{-1} , which has been selected here in lieu of τ_{insp} in order to more effectively depict binaries that show no appreciable change in their separation over the duration of the simulations. The values in the colorbar are normalized to the analytical BH stopping time given in Equation 4. The pink color palette corresponds to binaries that tighten ($\tau_{\text{insp}}^{-1} > 0$), while the blue color palette shows binaries that soften ($\tau_{\text{insp}}^{-1} < 0$). Small absolute frequencies, $|\tau_{\text{insp}}^{-1}|$ correspond to binaries experiencing a slower rates of change for both tightening and softening. The symbols in white depict binaries that experience no appreciable change (within simulation errors) in their orbital separation ($\tau_{\text{insp}}^{-1} \rightarrow 0$) and thus demarcate transitional flow conditions in the (ε_ρ, a_0) plane.

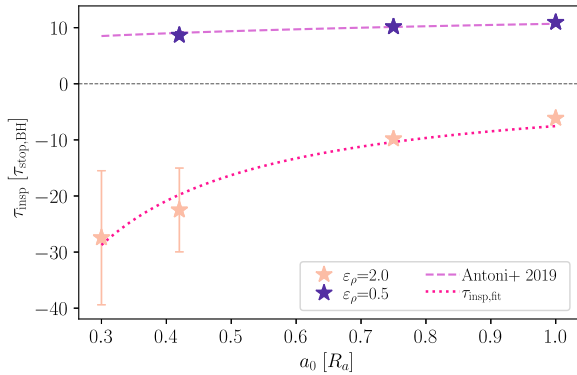


Figure 4. Orbit-averaged inspiraling timescale as a function of a_0 given by Equation 17. Values are normalized to the analytical BH stopping time given in Equation 4. For $\epsilon_\rho = 0.5$, $\tau_{\text{insp}} > 0$, while for $\epsilon_\rho = 2$, $\tau_{\text{insp}} < 0$. A positive timescale corresponds to an orbital tightening, while a negative timescale corresponds to an orbital widening. An increase in the absolute value of τ_{insp} is associated with a decrease in the rate of orbital tightening or widening. A least-squares fit to a power law of the form $\propto (a_0/R_a)^B$ is performed. The shallow density gradient models ($\epsilon_\rho = 0.5$) are compared with the trend $(a_0/R_a)^{0.19}$ found by Antoni et al. (2019). For the case where $\epsilon_\rho = 2.0$, $\tau_{\text{insp}} \propto (a_0/R_a)^{-1.1}$. This implies that binaries embedded in steep stellar density gradients will soften at a rate that progressively increases as a expands.

Figure 4 shows that for $\epsilon_\rho < 1$, binaries harden, while softening takes place when $\epsilon_\rho > 1.0$. We note that this transition also depends on a_0 albeit weakly compared to ϵ_ρ . In the presence of a steep density gradient, the two members of the binary spiral out as the flow transfers angular momentum to the system. For a fixed ϵ_ρ , the long term evolution of a binary system can be envisioned by moving along vertically in the (ϵ_ρ, a_0) plane. As observed in Figure 4 for the $\epsilon_\rho = 0.5$ case and discussed by Antoni et al. (2019) for the $\epsilon_\rho = 0$ case, the decrease in τ_{insp} with a indicates that gaseous drag forces in shallow density gradients can drive binaries to coalescence or to the critical separation at which gravitational wave radiation controls their subsequent orbital evolution. In contrast, for steeper density gradients ($\epsilon_\rho > 1$) we find that as the two binary members recede, the rate of softening increases, hastening the potential for tidal breakup. Given that for most CE flows $\epsilon_\rho \gtrsim 1$ (Everson et al. 2020), we thus conclude that binaries spiraling within CEs become less bound and are more vulnerable to be torn apart by tidal interactions as they fall closer to the primary’s core.

4.5. The Assembly of PSR J0337+1715

The evolution of triples is likely to be important for the formation of compact and exotic binaries. The evolution of a triple system with a mass-transferring outer star has been invoked to explain the triple system PSR J0337+1715 (Tauris & van den Heuvel 2014; Sabach & Soker 2015), which hosts a millisecond pulsar and two white dwarfs. This system is

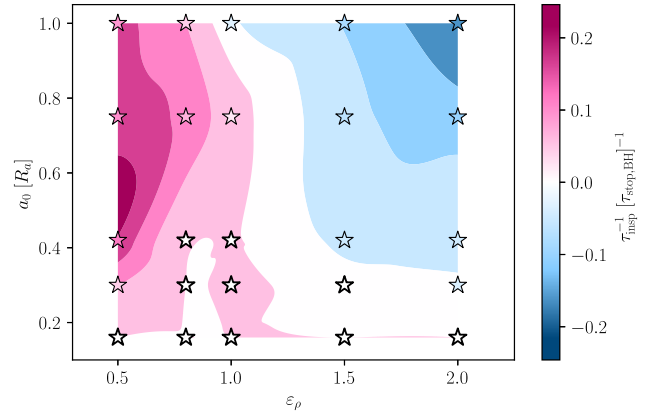


Figure 5. The orbit-averaged frequency τ_{insp}^{-1} in the (a_0, ϵ_ρ) plane for a binary with $q = 0.15$. τ_{insp}^{-1} provides an estimate of the ratio between the change in binary separation Δa averaged over an orbital period and the initial separation a_0 . The orbit-averaged frequency τ_{insp}^{-1} is selected here to better illustrate cases that, over the duration of the simulation, show no appreciable change in their separation. For such cases, $\tau_{\text{insp}}^{-1} \approx 0$. Values in the colorbar are given in units of the analytical BH stopping time given in Equation 4. The pink colors values show binaries that are tightened by the interaction with the CE flow ($\tau_{\text{insp}}^{-1} > 0$), while blue colors show binaries that become less gravitationally bound ($\tau_{\text{insp}}^{-1} < 0$). The darker colors mark binaries that experience a larger change in Δa over an orbital period. The white symbols show cases where $\Delta a \approx 0$ within the simulation errors and thus mark the transition between binary hardening and binary softening.

used in Section 2.2 to frame the typical flow conditions encountered by embedded CE binaries and argued that they are indeed representative of the bulk population of CE interactions (Everson et al. 2020).

To contextualize our numerical results (Figure 5) in the context of PSR J0337+1715 we find that ϵ_ρ in the envelope of the outer star varies between roughly 0.98 and 1.63 as a function of the distance from the center of mass of the evolving massive stellar progenitor. The reader is referred to Figure 7 in Appendix A for further details. This illustrates that the CE properties encounter by the embedded binary progenitor system resides on the right side of the parameter space explored in Figure 5. This in turn suggests that the embedded binary will soften and will become more vulnerable to tidal disruption. This provides credence to the idea by Sabach & Soker (2015) that tidal breakup of the binary can alter the hierarchical layout of this system. Based on the results of this work, we predict that binary splitting is inevitable and that the softening of the binary as it spirals near the tidal radius will only aid breakup.

5. SUMMARY AND CONCLUDING REMARKS

Field stars are commonly formed in pairs, and a fraction of these binaries are part of triple systems. Some binary members are expected to endure mass exchanges and can, mainly

during a phase of unstable mass transfer, spiral into the interior layers of the evolving star under the influence of drag from the surrounding envelope material. The associated drag forces deposit orbital kinetic energy into the envelope and are expected to influence the orbital configuration of the infalling binary, whose evolution had remain not well known.

In this paper we present a set of simulations that model a binary system as it becomes embedded into the CE of their tertiary. We approach this problem by running local hydrodynamic simulation in a wind tunnel setup and focus on a range of parameters informed by observations of hierarchical triple systems. We study the forces on the center of mass of the binary with contributions from dynamical friction and accretion of linear momentum. These numerical experiments have the advantage of being sufficiently controlled that we can gain full confidence in the numerical implementation and intuition for the effects of key variables. Our calculations have indicated that the structure of a CE has dramatic importance in shaping the properties of the embedded binary. Some key findings of this work are as follows.

- The forces on the center of mass of the binary are found to be comparable in magnitude and direction to those experienced by an effective star of mass m at the center of mass of the inner binary. We thus infer that the binary will sink into the envelope at a rate comparable to that previously found for single point masses (MacLeod et al. 2017a).
- The net accretion rate of the two bodies sees a reduction compared to that of a single point mass, which can be readily explained by the difference in accretion cross sections.
- The orbital evolution of binaries embedded in shallow density gradients ($\varepsilon_\rho < 0.5$) is found to follow the scaling with separation derived by Antoni et al. (2019) for a constant density medium ($\varepsilon_\rho \approx 0$). Such density gradients are not commonly found in the interiors of evolving stars.
- In contrast to the uniform density case, the binary orbital separation is found to increase with time for $\varepsilon_\rho > 1$. This causes binaries in CEs to soften and prevents them from subsequently merging. For these customary CE properties, the binary softens and the magnitude of the timescale decreases as the separation increases, which subsequently accelerates the softening. We conclude that for realistic CE conditions, embedded binaries will soften thus aiding disruption and ejection.

This study addresses a critical stage in the evolution of hierarchical triple systems: common envelope episodes. Given that multiple star systems are ubiquitous, we urgently need a more detailed understanding of the binary-star interaction channels to be able to more effectively decipher how the majority of triple systems evolve. This work tackles key aspects of the basic physics of binary-CE interactions. Triple systems might be interesting sources for LIGO progenitors (e.g., Vigna-Gómez et al. 2021) and might be central to understanding type Ia supernova explosions (e.g., Rajamuthukumar et al. 2023), and without a detailed understanding of CE, it might not be feasible to precisely determine the distribution of their properties.

We acknowledge use of the lux supercomputer at UC Santa Cruz, funded by NSF MRI grant AST 1828315. The 3D hydrodynamics software used in this work was developed in part by the DOE NNSA- and DOE Office of Science-supported Flash Center for Computational Science at the University of Chicago and the University of Rochester. E.R.-R. acknowledges support by the Heising-Simons Foundation and the NSF (AST-2307710, AST-2206243, AST-1911206, and AST-1852393). R.Y. is grateful for support from a Doctoral Fellowship from the University of California institute for Mexico and the United States (UCMEXUS) and the Consejo Nacional de Ciencia y Tecnología (CONACyT), a Texas Advanced Computing Center (TACC) Frontera Computational Science Fellowship, and a NASA FINESST award (21-ASTRO21-0068). A.M.-B. is supported by NASA through the NASA Hubble Fellowship grant HST-HF2-51487.001-A awarded by the Space Telescope Science Institute, which is operated by the Association of Universities for Research in Astronomy, Inc., for NASA, under contract NAS5-26555. R.W.E. acknowledges the support of the University of California President’s Dissertation-Year Fellowship, the Heising-Simons Foundation, the Vera Rubin Presidential Chair for Diversity at UCSC, and the National Science Foundation Graduate Research Fellowship Program under Grant No. 1339067. A.A. gratefully acknowledges support from the University of California, Dissertation-Year Fellowship, the Maria Cranor Fellowship at U.C. Berkeley, the National Science Foundation Graduate Research Fellowship under Grant No. DGE 1752814, and the Gordon and Betty Moore Foundation through Grant GBMF5076.

Software: FLASH 4.3 (Fryxell et al. 2000), MESA (Buchler & Yueh 1976; Fuller et al. 1985; Iglesias & Rogers 1993; Oda et al. 1994; Saumon et al. 1995; Iglesias & Rogers 1996; Itoh et al. 1996; Langanke & Martínez-Pinedo 2000; Timmes & Swesty 2000; Rogers & Nayfonov 2002; Irwin 2004; Ferguson et al. 2005; Cassisi et al. 2007; Chugunov et al. 2007; Cyburt et al. 2010; Potekhin & Chabrier 2010; Paxton et al. 2011, 2013, 2015, 2018, 2019; Jermyn et al. 2023), MESA SDK (Townsend 2021), yt (Turk et al. 2011)

A. COMMON ENVELOPE CONDITIONS IN TRIPLE SYSTEM PSR J0337+1715

The proposed post-CE formation scenario for PSR J0337+1715 begins with a primary massive main sequence star (*pink* star in Figure 6) orbiting a tight binary composed of two sun-like stars. As the outer massive star progenitor of PSR J0337+1715’s expands, it is speculated that the inner sun-like pair will be completely engulfed. As the binary spirals inside of the primary’s envelope, it is predicted to be tidally disrupted. This will result in the ejection of one of the sun-like companions (*orange* star in Figure 6). After the binary is tidally separated, the surviving companion (*light blue* star in Figure 6), continues to spiral in towards the primary’s He core, leading to the successful ejection of the H envelope. The post-CE configuration of the triple system is predicted to host a close binary, hosting the He core and the surviving sun-like companion, and the outer tertiary companion, which is expected to remain gravitationally bound. In what follows, we study the common envelope flow conditions that the binary will encounter during the CE phase.

Based on MESA models, here we calculate ε_ρ as a function of the radial distance from the core of the evolving primary star described in Section 2.2. When the primary enters the giant phase, the envelope will engulf the orbiting binary. This is the evolutionary phase that is key to the assembly of PSR J0337+1715 (Tauris & van den Heuvel 2014; Sabach & Soker 2015). We calculate that the primary will expand up to a radius of about $175 R_\odot$ during the asymptotic giant branch (Figure 1). For this representative model, we calculate the radial distance from the primary’s stellar core at which the binary becomes tidally disrupted. In this range of radii, we estimate the value of the density gradient parameter, ε_ρ , to be between 0.92 and 4.00. The results of this exercise are plotted in Figure 7. This value range of ε_ρ is indeed representative of most CE flow conditions (Everson et al. 2020).

As the binary, assumed to be composed of two $1 M_\odot$ sun-like stars (Section 2.2), spirals inside of the envelope depicted in Figure 7, it is expected to be tidally disrupted. We anticipate this to take place before the binary ($a = 60R_\odot$) reaches the innermost $70 R_\odot$ of the primary star (orange line in Figure 7). This will likely result, as envisioned by Sabach & Soker (2015), in the ejection of one of the sun-like companions. After the binary breakups, the bound companion will continue to spiral-in towards the primary’s core. We expect enough energy to be injected by the surviving companion to unbind the envelope before it reaches the tidal radius (yellow line in Figure 7).

B. STOPPING TIMESCALE

The stopping timescale, τ_{stop} , is a measure of the loss of kinetic energy of the center of mass of the binary (Equation 4). τ_{stop} in the CE context is a measure of how quickly the center of mass of the binary will spiral in towards the core of the evolving primary star. For our simulated binaries, we measure orbit-averaged stopping timescales. These are plotted in Figure 8. The values are normalized to the analytical solution for a single point mass found in Equation 4.

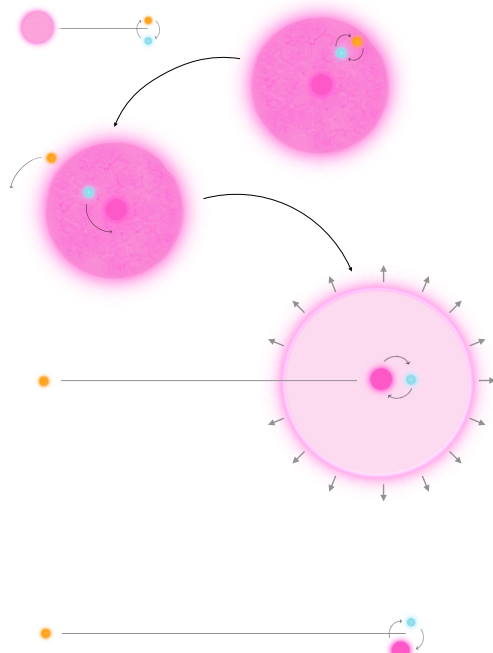


Figure 6. Diagram illustrating the proposed post-CE formation scenario for PSR J0337+1715 (Tauris & van den Heuvel 2014; Sabach & Soker 2015). The initial setup consists of three main-sequence stars: a primary (*pink*) with $M \approx 8M_\odot$, a secondary (*blue*) and a tertiary (*orange*) with $m_1 \approx m_2 \approx 1M_\odot$, where $M > m_1 + m_2$. As the primary evolves, it will expand and the system will undergo a CE. The center of mass of the binary will sink towards the core of the primary until it reaches its tidal radius. The tertiary is ejected from the CE but remains bound to the system, while the secondary sinks and unbinds the envelope. This results in a hierarchical triple system in which the inner binary is composed of the primary’s core and the secondary.

We see that the general trend is that the stopping timescale becomes shorter as ε_ρ increases. We can also see that stopping timescale remains pretty much constant with respect to the initial separation a_0 . The dissipation of the kinetic energy therefore depends primarily on the density gradient of the stellar profile. Our findings are in close agreement with the results of MacLeod et al. (2017a) for single point masses.

C. APPLICATION OF OUR RESULTS TO A BROAD RANGE OF EMBEDDED BINARIES

The characteristic Mach number of the flow \mathcal{M}_∞ is determined by ε_ρ and q (Equation 9). For most of the analysis in the study we have selected $q = 0.15$, inspired by the post-CE formation paradigm of PSR J0337+1715. Here we expand our analysis to include two different values of q . Figure 9 show the results of our study. We color the symbols depending on whether the final orbital separation is greater (*blue*) or smaller (*pink*) than a_0 . For binaries in which the separation increases (decreases), we label them as breaking

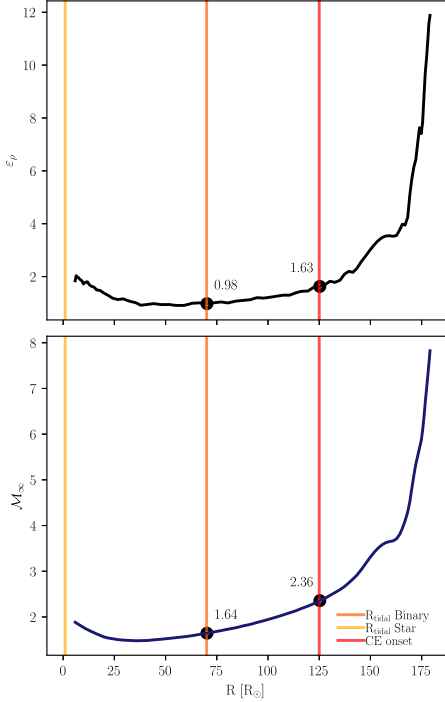


Figure 7. Common envelope flow conditions during the assembly of PSR J0337+1715. ε_ρ (top panel) and \mathcal{M}_∞ (bottom panel) as a function of radius from the centre of mass of the massive primary during the asymptotic giant branch. Yellow line represents the radius at which a $1 M_\odot$ sun-like star will become tidally disrupted, while the orange line shows the tidal disruption radius for the embedded binary ($a = 60R_\odot$). Red line shows the CE onset boundary as defined in MacLeod & Loeb (2020), implying that most of the material above this line will be lost before CE sets in.

(merging). The general trend observed here is similar for both $q = 0.10$ and $q = 0.15$. We observe a clear transition at around $\varepsilon_\rho = 1.0$, with steeper (shallower) density gradients causing binaries to soften (harden). The relation between \mathcal{M}_∞ , ε_ρ and q (Equation 9) is clearly displayed in Figure 9.

D. FLOW MORPHOLOGY

We illustrate here the morphology of the CE flow around the binary for the suite of simulations used in this study. We present snapshots of 9 different initial parameters. The snapshots are taken at the orbital plane ($z = 0$) and the colormap shows the density of the flow. The flow lines are drawn along velocity streamlines. Figure 10 plots nine different configurations of initial conditions. The three different columns from left to right show the change in initial semi-major axis: $a_0 = 0.16, 0.42, 1.0$. The three different rows show changes in ε_ρ : 0.5 (left), 1.0 (middle), and 2.0 (right). For the cases where the binary separation is the smallest, we see a clearly defined spiral shock structure. This is likely due to the bodies orbiting one another much faster than the flow crossing time.

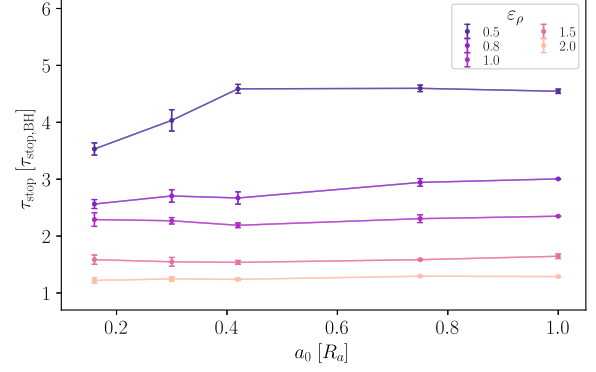


Figure 8. Stopping timescale for a binary with $q = 0.15$, embedded in a CE flow of varying physical conditions. Values are normalized by $\tau_{\text{stop,BH}}$ as in Equation 4. The colors represent the different values of the density gradient parameter: ε_ρ . The trend shows that the stopping timescale of the center of mass of the binary decreases as ε_ρ increases, so the center of mass of the binary will spiral-in faster into the CE. We find τ_{stop} to remain pretty constant regardless of the initial separation of the binary.

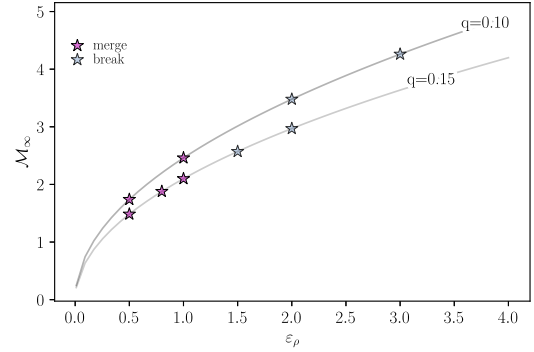


Figure 9. The evolution of binaries in the $(\varepsilon_\rho, \mathcal{M}_\infty)$ plane using numerical results from the simulations presented in this study. The relation between \mathcal{M}_∞ , ε_ρ and q (Equation 9) is shown for $q = 0.10$ and $q = 0.15$ (grey lines). The blue (pink) symbols show cases where binaries harden (soften) as they interact with the CE flow.

As the value of ε_ρ increases, the flow is observed to exhibit significantly variability imprinted at the smallest scales. This takes place as vortices shed in the wake cause some degree of breathing and instability of the location of the bow shock. Since this flow instability is not observed in the shallower-gradient cases (MacLeod et al. 2017a), the resultant drag force is much less variable. What is more, for large ε_ρ , there is a decrease in concentration of gas around the sinks, which drastically decreases the torque pushing the binary inwards (Antoni et al. 2019). The majority of the net torque pushing the binary outwards is generated at larger scales, of the order of the shock standoff distance.

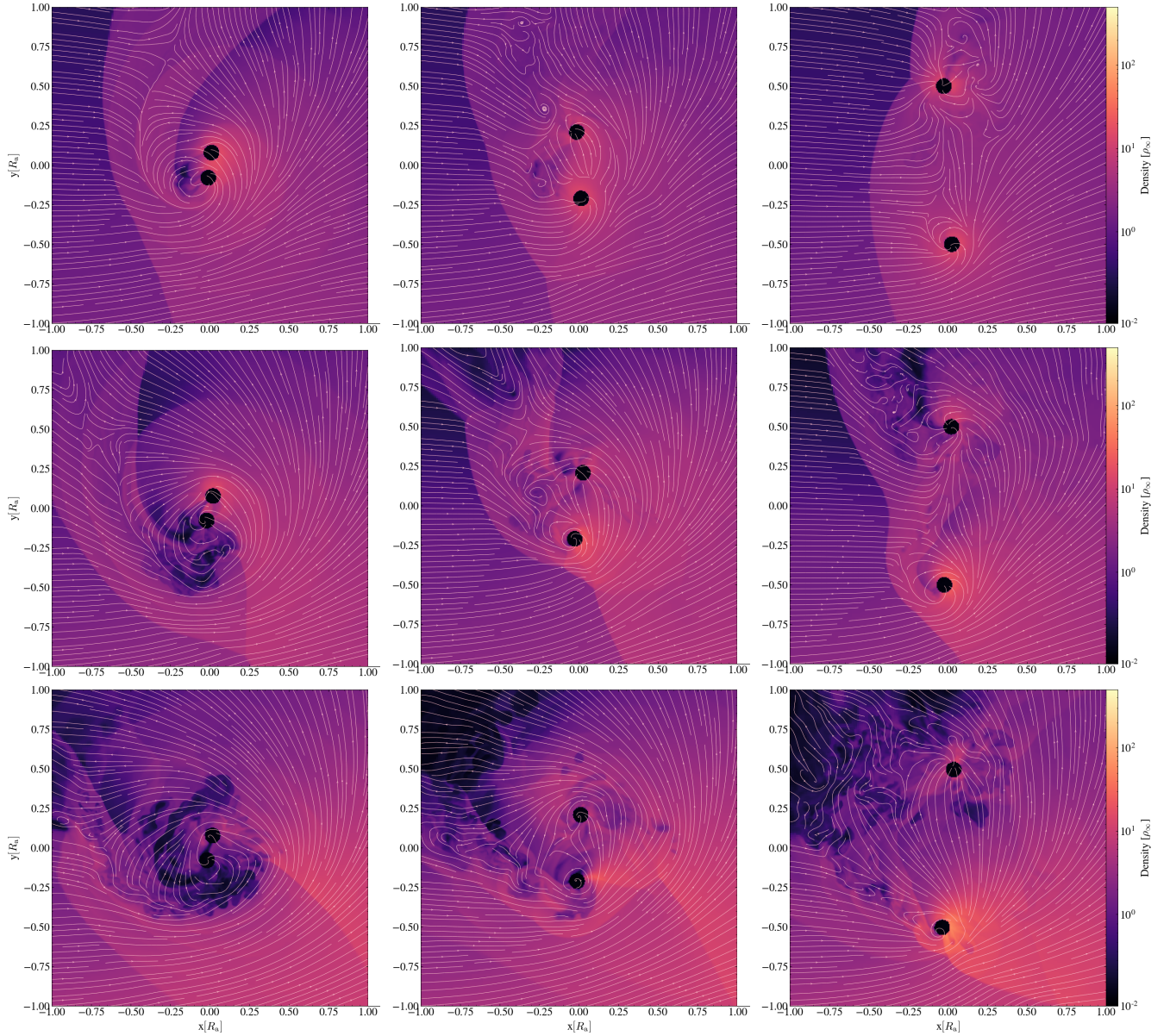


Figure 10. Flow morphology around the binary for the suite of simulations used in this study. Colormaps show the density of the flow in the orbital plane. The three different columns from left to right show the change in semi-major axis: $a_0 = 0.16, 0.42, 1.0$. The three different rows show the change in the flow driven by changes in ε_ρ : 0.5 (left), 1.0 (middle), and 2.0 (right).

REFERENCES

- Antoni, A., MacLeod, M., & Ramirez-Ruiz, E. 2019, *ApJ*, 884, 22, doi: [10.3847/1538-4357/ab3466](https://doi.org/10.3847/1538-4357/ab3466)
- Archibald, A. M., Gusinskaia, N. V., Hessels, J. W. T., et al. 2018, *Nature*, 559, 73, doi: [10.1038/s41586-018-0265-1](https://doi.org/10.1038/s41586-018-0265-1)
- Bondi, H., & Hoyle, F. 1944, *MNRAS*, 104, 273, doi: [10.1093/mnras/104.5.273](https://doi.org/10.1093/mnras/104.5.273)
- Bonnell, I. A., Bate, M. R., & Vine, S. G. 2003, *Monthly Notices of the Royal Astronomical Society*, 343, 413–418, doi: [10.1046/j.1365-8711.2003.06687.x](https://doi.org/10.1046/j.1365-8711.2003.06687.x)
- Buchler, J. R., & Yuch, W. R. 1976, *ApJ*, 210, 440, doi: [10.1086/154847](https://doi.org/10.1086/154847)
- Cassisi, S., Potekhin, A. Y., Pietrinferni, A., Catelan, M., & Salaris, M. 2007, *ApJ*, 661, 1094, doi: [10.1086/516819](https://doi.org/10.1086/516819)
- Chugunov, A. I., Dewitt, H. E., & Yakovlev, D. G. 2007, *PhRvD*, 76, 025028, doi: [10.1103/PhysRevD.76.025028](https://doi.org/10.1103/PhysRevD.76.025028)
- Colella, P., & Woodward, P. R. 1984, *Journal of Computational Physics*, 54, 174, doi: [10.1016/0021-9991\(84\)90143-8](https://doi.org/10.1016/0021-9991(84)90143-8)
- Comerford, T. A. F., & Izzard, R. G. 2020, *MNRAS*, 498, 2957, doi: [10.1093/mnras/staa2539](https://doi.org/10.1093/mnras/staa2539)
- Cyburtt, R. H., Amthor, A. M., Ferguson, R., et al. 2010, *ApJS*, 189, 240, doi: [10.1088/0067-0049/189/1/240](https://doi.org/10.1088/0067-0049/189/1/240)
- Everson, R. W., Hutchinson-Smith, T., Vigna-Gómez, A., & Ramirez-Ruiz, E. 2023, arXiv e-prints, arXiv:2310.08658, doi: [10.48550/arXiv.2310.08658](https://doi.org/10.48550/arXiv.2310.08658)
- Everson, R. W., MacLeod, M., De, S., Macias, P., & Ramirez-Ruiz, E. 2020, *ApJ*, 899, 77, doi: [10.3847/1538-4357/aba75c](https://doi.org/10.3847/1538-4357/aba75c)
- Federrath, C., Banerjee, R., Clark, P. C., & Klessen, R. S. 2010, *ApJ*, 713, 269, doi: [10.1088/0004-637X/713/1/269](https://doi.org/10.1088/0004-637X/713/1/269)
- Ferguson, J. W., Alexander, D. R., Allard, F., et al. 2005, *ApJ*, 623, 585, doi: [10.1086/428642](https://doi.org/10.1086/428642)
- Fryxell, B., Olson, K., Ricker, P., et al. 2000, *ApJS*, 131, 273, doi: [10.1086/317361](https://doi.org/10.1086/317361)
- Fuller, G. M., Fowler, W. A., & Newman, M. J. 1985, *ApJ*, 293, 1, doi: [10.1086/163208](https://doi.org/10.1086/163208)
- Glanz, H., & Perets, H. B. 2021a, *MNRAS*, 500, 1921, doi: [10.1093/mnras/staa3242](https://doi.org/10.1093/mnras/staa3242)
- . 2021b, *MNRAS*, 507, 2659, doi: [10.1093/mnras/stab2291](https://doi.org/10.1093/mnras/stab2291)
- Hoyle, F., & Lyttleton, R. A. 1939, *Mathematical Proceedings of the Cambridge Philosophical Society*, 35, 405–415, doi: [10.1017/S0305004100021150](https://doi.org/10.1017/S0305004100021150)
- Iglesias, C. A., & Rogers, F. J. 1993, *ApJ*, 412, 752, doi: [10.1086/172958](https://doi.org/10.1086/172958)
- . 1996, *ApJ*, 464, 943, doi: [10.1086/177381](https://doi.org/10.1086/177381)
- Irwin, A. W. 2004, *The FreeEOS Code for Calculating the Equation of State for Stellar Interiors*. <http://freeeos.sourceforge.net/>
- Itoh, N., Hayashi, H., Nishikawa, A., & Kohyama, Y. 1996, *ApJS*, 102, 411, doi: [10.1086/192264](https://doi.org/10.1086/192264)
- Jermyn, A. S., Bauer, E. B., Schwab, J., et al. 2023, *ApJS*, 265, 15, doi: [10.3847/1538-4365/acae8d](https://doi.org/10.3847/1538-4365/acae8d)
- Lagos, F., Zorotovic, M., Schreiber, M. R., & Gänsicke, B. T. 2023, *MNRAS*, 519, 2302, doi: [10.1093/mnras/stac3675](https://doi.org/10.1093/mnras/stac3675)
- Langanke, K., & Martínez-Pinedo, G. 2000, *NuPhA*, 673, 481, doi: [10.1016/S0375-9474\(00\)00131-7](https://doi.org/10.1016/S0375-9474(00)00131-7)
- Law-Smith, J. A. P., Everson, R. W., Ramirez-Ruiz, E., et al. 2020, arXiv e-prints, arXiv:2011.06630. <https://arxiv.org/abs/2011.06630>
- MacLeod, M., Antoni, A., Murguía-Berthier, A., Macias, P., & Ramirez-Ruiz, E. 2017a, *The Astrophysical Journal*, 838, 56, doi: [10.3847/1538-4357/aa6117](https://doi.org/10.3847/1538-4357/aa6117)
- MacLeod, M., & Loeb, A. 2020, *The Astrophysical Journal*, 895, 29, doi: [10.3847/1538-4357/ab89b6](https://doi.org/10.3847/1538-4357/ab89b6)
- MacLeod, M., Macias, P., Ramirez-Ruiz, E., et al. 2017b, *ApJ*, 835, 282, doi: [10.3847/1538-4357/835/2/282](https://doi.org/10.3847/1538-4357/835/2/282)
- MacLeod, M., & Ramirez-Ruiz, E. 2015a, *ApJ*, 803, 41, doi: [10.1088/0004-637X/803/1/41](https://doi.org/10.1088/0004-637X/803/1/41)
- . 2015b, *ApJL*, 798, L19, doi: [10.1088/2041-8205/798/1/L19](https://doi.org/10.1088/2041-8205/798/1/L19)
- Michaely, E., & Perets, H. B. 2019, *MNRAS*, 484, 4711, doi: [10.1093/mnras/stz352](https://doi.org/10.1093/mnras/stz352)
- Moe, M., & Di Stefano, R. 2017, *The Astrophysical Journal Supplement Series*, 230, 15, doi: [10.3847/1538-4365/aa6fb6](https://doi.org/10.3847/1538-4365/aa6fb6)
- Murguía-Berthier, A., MacLeod, M., Ramirez-Ruiz, E., Antoni, A., & Macias, P. 2017, *ApJ*, 845, 173, doi: [10.3847/1538-4357/aa8140](https://doi.org/10.3847/1538-4357/aa8140)
- Oda, T., Hino, M., Muto, K., Takahara, M., & Sato, K. 1994, *Atomic Data and Nuclear Data Tables*, 56, 231, doi: [10.1006/adnd.1994.1007](https://doi.org/10.1006/adnd.1994.1007)
- Paxton, B., Bildsten, L., Dotter, A., et al. 2011, *ApJS*, 192, 3, doi: [10.1088/0067-0049/192/1/3](https://doi.org/10.1088/0067-0049/192/1/3)
- Paxton, B., Cantiello, M., Arras, P., et al. 2013, *ApJS*, 208, 4, doi: [10.1088/0067-0049/208/1/4](https://doi.org/10.1088/0067-0049/208/1/4)
- Paxton, B., Marchant, P., Schwab, J., et al. 2015, *ApJS*, 220, 15, doi: [10.1088/0067-0049/220/1/15](https://doi.org/10.1088/0067-0049/220/1/15)
- Paxton, B., Schwab, J., Bauer, E. B., et al. 2018, *ApJS*, 234, 34, doi: [10.3847/1538-4365/aaa5a8](https://doi.org/10.3847/1538-4365/aaa5a8)
- Paxton, B., Smolec, R., Schwab, J., et al. 2019, *ApJS*, 243, 10, doi: [10.3847/1538-4365/ab2241](https://doi.org/10.3847/1538-4365/ab2241)
- Potekhin, A. Y., & Chabrier, G. 2010, *Contributions to Plasma Physics*, 50, 82, doi: [10.1002/ctpp.201010017](https://doi.org/10.1002/ctpp.201010017)
- Rajamuthukumar, A. S., Hamers, A. S., Neunteufel, P., Pakmor, R., & de Mink, S. E. 2023, *ApJ*, 950, 9, doi: [10.3847/1538-4357/acc86c](https://doi.org/10.3847/1538-4357/acc86c)
- Ransom, S. M., Stairs, I. H., Archibald, A. M., et al. 2014, *Nature*, 505, 520, doi: [10.1038/nature12917](https://doi.org/10.1038/nature12917)
- Rogers, F. J., & Nayfonov, A. 2002, *ApJ*, 576, 1064, doi: [10.1086/341894](https://doi.org/10.1086/341894)

- Sabach, E., & Soker, N. 2015, *Monthly Notices of the Royal Astronomical Society*, 450, 1716, doi: [10.1093/mnras/stv717](https://doi.org/10.1093/mnras/stv717)
- Saumon, D., Chabrier, G., & van Horn, H. M. 1995, *ApJS*, 99, 713, doi: [10.1086/192204](https://doi.org/10.1086/192204)
- Soker, N., & Bear, E. 2021, *MNRAS*, 505, 4791, doi: [10.1093/mnras/stab1561](https://doi.org/10.1093/mnras/stab1561)
- Tauris, T. M., & van den Heuvel, E. P. J. 2014, *The Astrophysical Journal*, 781, L13, doi: [10.1088/2041-8205/781/1/L13](https://doi.org/10.1088/2041-8205/781/1/L13)
- Timmes, F. X., & Swesty, F. D. 2000, *ApJS*, 126, 501, doi: [10.1086/313304](https://doi.org/10.1086/313304)
- Toonen, S., Hamers, A., & Zwart, S. P. 2016, The evolution of hierarchical triple star-systems. <https://arxiv.org/abs/1612.06172>
- Townsend, R. 2021, MESA SDK for Linux, 21.4.1, Zenodo, doi: [10.5281/zenodo.5802444](https://doi.org/10.5281/zenodo.5802444)
- Turk, M. J., Smith, B. D., Oishi, J. S., et al. 2011, *ApJS*, 192, 9, doi: [10.1088/0067-0049/192/1/9](https://doi.org/10.1088/0067-0049/192/1/9)
- van den Heuvel, E. P. J. 1976, in *Structure and Evolution of Close Binary Systems*, ed. P. Eggleton, S. Mitton, & J. Whelan, Vol. 73, 35
- Vigna-Gómez, A., Toonen, S., Ramirez-Ruiz, E., et al. 2021, *ApJL*, 907, L19, doi: [10.3847/2041-8213/abd5b7](https://doi.org/10.3847/2041-8213/abd5b7)
- Webbink, R. F. 1984, *ApJ*, 277, 355, doi: [10.1086/161701](https://doi.org/10.1086/161701)
- Wu, S., Everson, R. W., Schneider, F. R. N., Podsiadlowski, P., & Ramirez-Ruiz, E. 2020, *ApJ*, 901, 44, doi: [10.3847/1538-4357/abaf48](https://doi.org/10.3847/1538-4357/abaf48)